JMEPEG (2022) 31:8068–8083
https://doi.org/10.1007/s11665-022-06814-4

1059-9495/$19.00

TECHNICAL ARTICLE

Digital Prognosis of Fatigue Residual Life of Lightweight Metallic Materials

Yali Yang, Hao Chen, Jiwen Li, Wei Liu, Xuefei Shi, Qiuwei He, Yujie Liu, and Jie Shen

Submitted: 20 November 2021 / Revised: 13 February 2022 / Accepted: 18 February 2022 / Published online: 30 March 2022

Fatigue damage of critical components and structures is an important phenomenon in engineering practice where service loads are normally much lower than the strength of materials. Few past studies focused on the correlation between macroscopic fatigue residual life and the micro-/meso-scale defect evolution He (Fatigue Fract. Eng. Mater. Struct. 36: 102-114, 2013), Shanyavskiy (AIP Conf. Proc. 2167: 020324, 2019), Tang (Int. J. Fatigue 70: 270 277, 2015). This study explores the fatigue damage with three significant contributions: (1) one of the first studies on predicting fatigue residual life at different load stages without prior knowledge of the load history, (2) a new multiscale fatigue damage index for linking of micro-/meso-scale defects and damage to macroscale high-cycle fatigue life, and (3) a novel incremental evaluation method for fatigue damage. A series of coordinated materials tests were conducted along with the corresponding numerical simulations. Experimental results indicate that our multiscale fatigue damage index (MFDI) is significantly better than the state of the art in terms of the correlation with actual fatigue life of test specimens and MFDI may serve as an ideal fatigue damage signature for nondestructive inspection of fatigue residual life. Our MFDI can also be potentially utilized to evaluate the impact of micro-/meso-scale defects and damage in new manufacturing processes of materials such as additive manufacturing and nanomaterials manufacturing.

Keywords additive manufacturing, fatigue damage, fatigue life, lightweight materials, materials defects, microstructure, nanomaterials

1. Introduction

Fatigue damage and related life are crucial to the safety of important products or infrastructures in engineering practice where the service loads are frequently much lower than the strength of materials. Although many studies have been conducted on the fatigue damage and life at either macroscale or microscale, few focused on the correlation between macroscopic fatigue life and the micro-/meso-scale defect evolution (Ref 1-3). Existing stress-life or strain-life models presume that the load history of components or structures is known. It would be a daunting task to record an entire load history over 10 years. Then, a natural question to ask is "Can the residual life of a component be predicted without knowing its load history?"

Additive manufacturing and nanomaterials manufacturing represent a trend of developing or manufacturing new materials in the 21st century. However, the drawbacks of current 3D printing technologies include (1) defects introduced during the printing process, and (2) larger variation of the material properties. In order to quantify the fatigue performance of parts manufactured from 3D printing processes, another question that we would like to ask is "Can we predict the fatigue life of a component with many microscale defects embedded from a 3D printing process?"

The aforementioned problems and challenges call for a study on a new methodology to precisely predict the fatigue life of components or structures without knowing load history information and without assuming that the manufactured material is defect free.

2. Literature Review

Fatigue of engineering materials is caused by gradual material degradation under cyclic loads that are smaller than the material yield strength. Studies on fatigue dated back to 1837 when Wilhelm Albert developed a test machine for conveyor chains (Ref 4). Over the years, different concepts and methods were introduced to address this important problem. A log-log relationship for S-N (stress-life) curve was proposed by O. H. Basquin in 1910 via using Wöhler's test data (Ref 5). Because of the proportionality between stress and strain in elasticity, high-cycle fatigue can also be approximated by an ε-N (strain-life) curve. Complex loading can be decomposed into a series of simple cyclic loading via a rainflow counting algorithm (Ref 6). Miner (Ref 7) proposed a Miner's rule to account for the accumulative damage of different stress levels. A critical plane method was developed by Brown and Miller (Ref 8) for handling the fatigue life under multiaxial conditions. Both tension and shear loads on this plane should be considered. Furthermore, the effect of mean stress on fatigue damage can be

Yali Yang and **Hao Chen**, Shanghai University of Engineering Science, Shanghai, China; **Jiwen Li** and **Wei Liu**, Henan University of Science and Technology, Luoyang, China; **Xuefei Shi**, Beijing University of Science and Technology, Beijing, China; **Qiuwei He**, Jilin University, Changchun, China; **Yujie Liu**, Southwest Jiaotong University, Chengdu, China; and **Jie Shen**, University of Michigan, Dearborn, Michigan. Contact e-mail: shen@umich.edu.

corrected by several methods, including Morrow's method (Ref 9).

Coffin and Manson explained a fatigue crack-growth in terms of plastic strain at the crack tips. Coffin-Manson law (Ref 10-13) reveals that the number of cycles to fracture in low-cycle fatigue is related to the amplitude of cyclic plastic deformation.

In fracture mechanics approaches (ΔK or ΔJ), a macro-crack is normally considered, and it likely corresponds to a very late stage of the entire fatigue damage process before rupture. The critical plane approach (Ref 10, 14) can be used to predict the crack propagation direction. Damage mechanics is another way to predict the behavior of fatigue damage accumulation (Ref 15-18). In these methods, damage variables were used as internal state variables for characterizing the progressive degradation of materials (Ref 15, 17-24). In conventional micromechanics, materials defects are frequently simplified as spheres or ellipsoids. Such inaccurate simplification can provide only a low-quality estimation of the mechanical properties of materials. Since cracks and smoothly shaped voids play a totally different role in materials degradation, porosity is indeed an inaccurate metric for fatigue damage.

All the aforementioned approaches demand the load history as a precondition to predict fatigue residual life. This may not be easily realized in engineering practice over a timespan of 10 years for many components or structures. To acquire the material degradation state at any service point, several nondestructive methods were used, including ultrasonic wave propagation (Ref 25-27), vibration (Ref 28), and acoustic emission (Ref 29-31). But, these methods are not precise in describing exact spatial damage distribution. Some two-dimensional image processing protocols (Ref 32-34) and three-dimensionally reconstructed microstructures (Ref 35-38) were based on single or serial cross-sectioning, which is not suited to investigating fatigue damage evolution. Three-dimensional computed tomography (gamma ray (Ref 39), neutron (Ref 40), synchrotron (Ref 40), ion beam (Ref 38), and x-ray (Ref 41-49)) were a more accurate method in determining the material defects. Unfortunately, little success has been reported in using the computed tomography data to accurately predict the macroscopic fatigue residual life via micro- and meso-scale materials defects in existing public literature (Ref 50-52).

Since the existing methods are inaccurate to predict the fatigue residual life of materials without prior knowledge of load history, the main objective of this paper is to develop an accurate methodology to predict the fatigue residual life of materials test specimens based on x-ray CT data without needing the information of load history. This methodology is crucial to any further development in multiscale nondestructive prognosis for the residual life of critical components or structures.

The rest of this paper is organized as follows. In section 3, the methodology of our approach is described. The introduction to coordinated materials testing is provided in section 4. The simulations and the analyses of experimental results are given in section 5, followed by some concluding remarks in section 6.

3. Methodology

Table 1 shows a flowchart of our main algorithm to this problem. There are several important technical components in this approach, as detailed in each sub-section.

3.1 A New Physical-Virtual System on Fatigue Life via Coordinated Materials Testing and Numerical Simulations

Our key idea is that material testing and x-ray scanning are interleaved for each test specimen during its high-cycle fatigue test. First, several specimens are tested to determine the fatigue life for a specified loading condition. Then, about five important loading stages are computed and each of those corresponds to a certain number of loading cycles such as 20,000 or 40,000 to cover the entire fatigue lifespan of the specimens. Next, a new multiscale fatigue damage index (MFDI) is computed, and a new incremental prognosis method is proposed to predict the residual life of the specimens. Last, a comparison is made with materials testing results.

3.2 A Voxel-based Denoising Method for CT Data

Measurement noise due to optical scattering or instrument vibration is an issue that may have an impact on the accuracy of reconstructed model. In this paper, a voxel-based method is proposed to perform a denoising process on the x-ray CT raw data, as described in Table 2. Herein, the denoising is a process that removes measurement noises generated from x-ray CT scans. Step 4 is useful only for the cases where light scattering is caused by surface roughness of the materials specimens. At the end of step4, MATERIAL and BOUNDARY elements are considered as material elements, BACKGROUND elements denote background space, and DEFECT elements refer to interior defects.

As to step 5, as long as there is no entire rupture in a material domain, we define the largest material volume as the domain for the material specimens. All the other smaller volumes are eliminated. Figure 1 demonstrates the effect of our method.

One benefit of our approach is the integration of x-ray data input, denoising, segmentation, and finite element meshing into a seamless process without labor-intensive editing. This is reflected by a new defect-sensitive volume reconstruction and meshing method in the next sub-section.

3.3 A New Defect-Sensitive Volume Reconstruction and Meshing Method

The projection data of x-ray scanning are first converted into a volume data model of the materials test specimens. It is essentially a stack of section images. When this volume model is transformed into a 3D finite element model, three issues need to be paid special attentions:

(1) Small voids and cracks should not be filled by some graphics processing softwareMany existing graphics algorithms tend to fill in small holes or cracks for the sake of visual perfection. In the context of material sciences, these small defects are vital information to determine which manufacturing process should be selected over other processes or over the same process with different manufacturing parameters. In this study, a special treatment of measuring the size of each defect was imposed to maintain those small material defects during simulations.
(2) Boundary smoothing should be avoided for the accurate analysis of crack propagation or damage evolutionThe boundary smoothing alters the stress concentration in a material domain. This will in turn affect the accuracy of predicting the fatigue life. In the cases where a remesh-

Table 1 An algorithm for computing a new multiscale fatigue damage index and fatigue life

Algorithm 1: computation of multiscale fatigue damage index and fatigue life	
Step 1	pretest materials specimens to experimentally estimate the fatigue life of specimens under a set of load conditions
Step 2	Determine critical load stages for an incremental coordinated physical-virtual test
Step 3	Loop over the critical load stages obtained from step 2
	Step 3.1 Read in x-ray CT data
	Step 32. Conduct a new voxel-based denoising process on CT data
	Step 3.3 Convert the CT data to volume model via a new defect-sensitive method
	Step 3.4 Compute our new multiscale fatigue damage index (MFDI)
	Step 3.4.1 Perform microscale finite element analysis in each representative volume element
	Step 3.4.2. Conduct macroscale finite element analysis on the material domain
	Step 3.5 Predict the residual life of materials via a new incremental prognosis method

Table 2 An algorithm for denoising x-ray CT data

Algorithm 2: denoising of x-ray CT data	
Step 1	Convert x-ray CT data to a 3d array
Step 2	Establish Element-element neighbor relation via face connection
Step 3	Remove all the elements with less than 2 face connections
Step 4	Use a scanline pass along each coordinate direction (positive and negative) to process noise caused by surface roughness.
	Label all the elements into two categories: DEFECT and MATERIAL
	Step 4.1 Scan along a coordinate direction, assigning the label of each element to BACKGROUND till an element with label MATERIAL is encountered
	Step 4.2 Change the label from MATERIAL to BOUNDARY
	Step 4.3 Change the label from MATERIAL to BOUNDARY if it is before the first BOUNDARY of the next line
Step 5	Conduct a volume propagation to remove small isolated material volumes

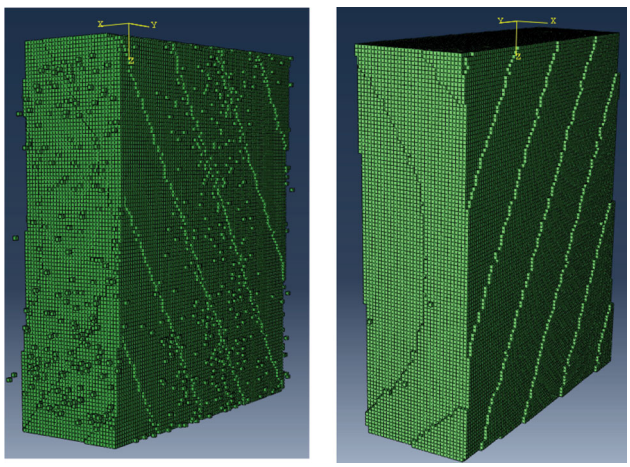

Fig. 1 The effect of our scan-line denoising algorithm

ing is needed, we developed a special feature-preserving remeshing algorithm, which is capable of maintaining the zigzagged features (Ref 53).

(3) Many existing software tools (Materialise 3-matic, ScanIP, DragonFly, ITK-snap, iso2mesh and Dream3D) are based on the processing of a set of 2D cross section imagesWhen a 3D model is processed, the procedure becomes tedious; for some other software tools (Mesh3D and VTK), a surface mesh is generated first. Normally, some small surfaces (voids or defects) will be lost. It needs to be connected to a volume meshing software like Hypermesh in a labor-intensive process.

In addition, with the fast advanced of x-ray computed tomography technology, the total number of voxels for each test specimen could be over 8 billion elements, which exceed the limit of 32-bit integers and cause a big data problem. Consequently, we propose a new defect-sensitive volume reconstruction and meshing method, as described in Table 3.

Mesh sensitivity is an important issue for any finite element analysis in which cracks are involved. In the cases where only a few large cracks exist, a nonlocal analysis can be applied as in our previous study (Ref 54). For the problem in this study, the number of materials defects is a variable, which is dependent upon mesh density and the original x-ray CT scanning resolution. It is difficult, if not impossible, to have a theoretical proof on the convergence of the finite element analyses with respect to mesh density because the number of materials defects dynamically changes with the mesh density. With different

Table 3 An algorithm for defect-sensitive volume reconstruction and meshing

Algorithm 3: defect-sensitive volume reconstruction and meshing method	
Step 1	Perform adaptive sampling of x-ray CT data based on our study on mesh density
Step 2	Construct a volume model via a scanline method without eliminating interior defects
Step 3	Reconstruct a free-form surface mesh model via the marching cube method without eliminating the surfaces of material defects
Step 4	Conduct a volume meshing via the wavefront method
Step 5	For calculating our multiscale fatigue damage index in Sect. 3.4, skip steps 1 through 4 Step 5.1 Mesh each representative volume element (RVE) independently at a fine level Step 5.2 Construct a volume model at a coarse level

mesh densities given in Figs 2 and 3 numerically shows the variation of maximum strain with respect to mesh density in the context of this study. A plateau is observed between 100,000 and 400,000 elements. The mesh domain in Fig. 2 corresponds to the middle section of material test specimens in Fig. 7 at the later part of this paper. If the number of finite elements is too small (e.g., less than 100,000), many material defects are filtered out; if the number of elements is too large (i.e., more than a million), the computed stress and strain become greater unless a nonlocal analysis is used. It is recommended that a mesh density of 0.5 to 1.0 million elements for a material domain to be investigated. The execution time of finite element analysis at different mesh densities is given in Fig. 3 as well.

Based on the above analysis on mesh density, the plateau in Fig. 3(a) and (b) represents a desired mesh density range to cover most defects within the domain of test specimens without incurring high computational costs. An adaptive sampling scheme (step 1 in Algorithm 3) is designed to convert a volume model with several billion elements to a simplified model with less than a million elements. The simplified model is still complex enough to retain a majority of defect features of the material domain, as illustrated in Fig. 4. This approach facilitates the comparison of our super representative volume element with the existing methods (the Brown-Miller model and principal stress/strain model for fatigue life).

In steps 3 and 4 of Algorithm 3, marching cube algorithm (Ref 55, 56) is implemented and directly coupled with a volume meshing algorithm (Ref 57) to form a seamless process without losing small voids/defects and without boundary smoothing. Figure 5 shows two results of running our method on small material defects. The left image of Fig. 5 depicts two small defects: One is located near a side surface, and the other is at an edge. The marching algorithm works properly in constructing the concave faces of the defects; the right image of Fig. 5 demonstrates a large irregular defect surface to show the effectiveness of surface meshing.

To compute our multiscale fatigue damage index in Sect. 3.4, multiple local microscale finite element mesh models are independently constructed for microscale analysis. Figure 6 illustrates the meshing models of three representative volume elements (RVEs) at different locations within a material domain and with different degrees of material damage. At a macroscopic level, only one integrated volume model is used for macroscale analysis.

The criterion to select the size of RVEs is that the minimum size should be 15x15x15 voxels. There is no upper bound for the size. Few limitations are the constraints from the memory, computational power and time.

3.4 A New Multiscale Fatigue Damage Index

The computation of our new multiscale fatigue damage index (MFDI) relies on the following two stages:

(1) A multiscale finite element analysis
(2) Formulation of MFDI at macroscopic scale

First, with a framework of multi-level finite element method, a direct multi-resolution analysis of volumetric material domain is used. At each fine level, only local finite element analyses are performed. Consequently, only local finite element meshes are needed on the fly in a sequential or parallel order. This solves a big data problem. For the small materials test specimens, two-scale bridging is sufficient. The mechanical property at microscale is estimated by Ref 58:

$$C^{\text{micro}}_{\text{ijpm}} = C^{\text{RVE}_k}_{ijpm} = \frac{1}{|V_{\text{micro}}|}\int\limits_{V_{\text{micro}}} C_{\text{ijkl}} L^{\text{micro}}_{\text{klpm}}\, dV_{\text{micro}} = \frac{1}{|V_{\text{RVE}_k}|}\int\limits_{V_{\text{RVE}_k}} C_{\text{ijkl}} L^{\text{RVE}_k}_{\text{klpm}}\, dV_{\text{RVE}_k}, \quad (k = 1, n), \tag{Eq 1a}$$

$$\begin{aligned}&\int\limits_{V_{\text{micro}}} C_{\text{ijpm}}\varepsilon_{ij}(v^{\text{micro}})\varepsilon^{qs}_{\text{pm}}(u^{\text{micro}})dV_{\text{micro}} \\ &= \int\limits_{V_{\text{RVE}_k}} C_{\text{ijpm}}\varepsilon_{ij}(v^{\text{RVE}_k})\varepsilon^{\text{qs}}_{\text{pm}}(u^{\text{RVE}_k})\text{d}V_{\text{RVE}_k} \\ &= \int\limits_{\partial V_{\text{micro}}} \lambda v_i^{\text{micro}}((u_i^{\text{micro}})^{\text{qs}} - (d_i^{\text{micro}})^{\text{qs}})\text{d}\partial V_{\text{micro}} \\ &= \int\limits_{\partial V_{\text{RVE}_k}} \lambda v_i^{\text{RVE}_k}((u_i^{\text{RVE}_k})^{\text{qs}} - (d_i^{\text{RVE}_k})^{qs})\text{d}\partial V_{RVE_k}, \quad (k = 1, n),\end{aligned} \tag{Eq 1b}$$

where superscript and subscript "micro" refers to quantities at the microscale. V_{RVE} is the domain of RVE (Representative Volume Element). RVE_k represents the k-th RVE in a test specimen or a structural domain. n is the number of sampling RVEs in Ω, which refers to the domain of a specimen or structure. C_{ijkl} represents a stiffness tensor, and L_{klpm} can be calculated by using a weak form of the RVE equilibrium equation:

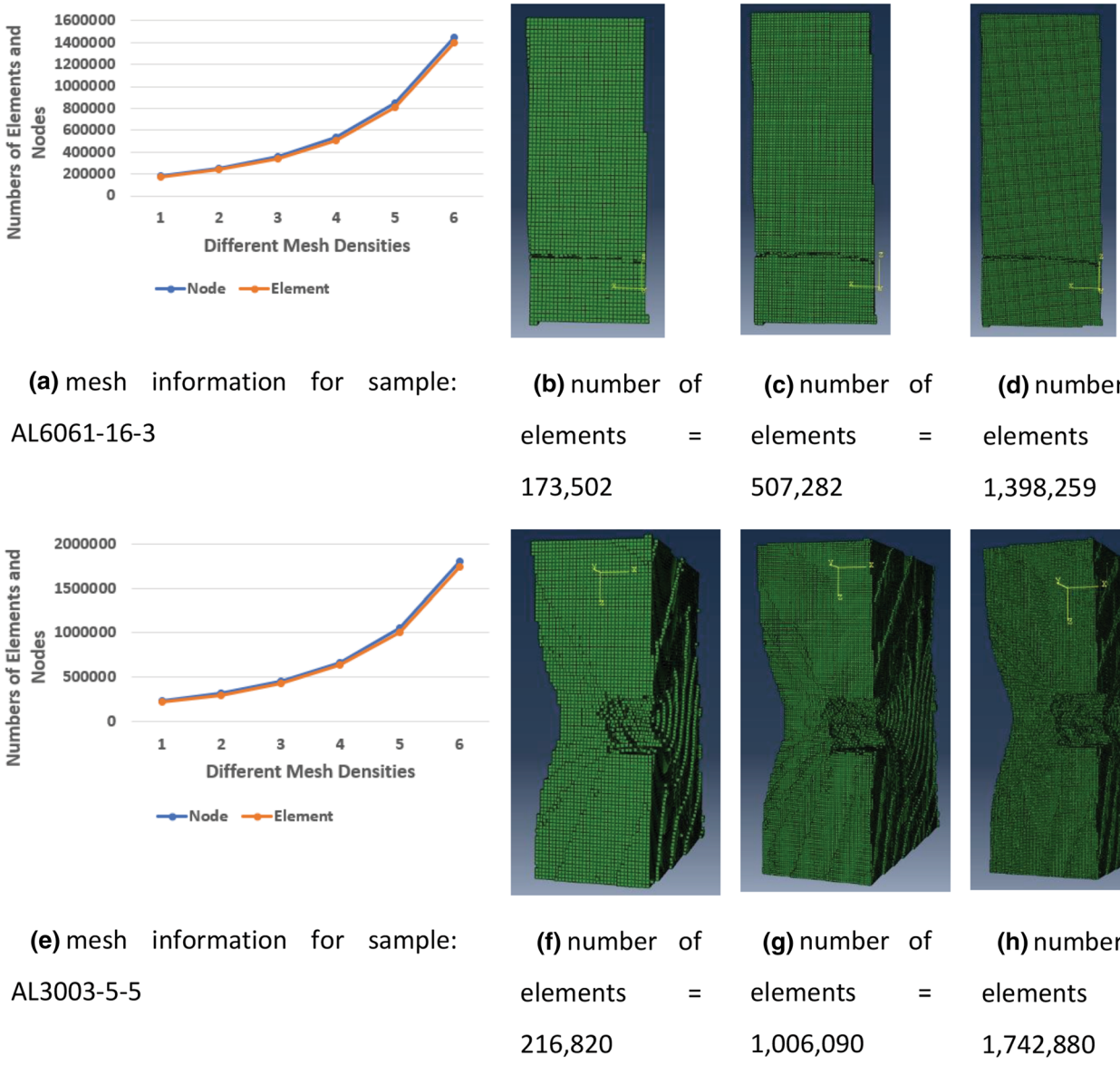

Fig. 2 Various mesh densities used to study mesh dependence

$$\int_{V_{\mathrm{RVE}_k}} C_{\mathrm{ijpm}}\varepsilon_{ij}(v)\varepsilon^{\mathrm{qs}}_{\mathrm{pm}}(u)\mathrm{d}V_{\mathrm{RVE}_k} = \int_{\partial V_{\mathrm{RVE}_k}} \lambda v_i(u_i^{qs} - d_i^{qs})\mathrm{d}\partial V_{RVE_k}, \quad (k = 1, n), \tag{Eq 1c}$$

where λ refers to a penalty parameter. u and v stand for the displacement and virtual displacement, respectively. d is the specified displacement, and ∂V refers to the boundary surface of V. $\varepsilon_{\mathrm{kl}} = L_{\mathrm{klpm}}\bar{\varepsilon}_{\mathrm{pm}}$. $\varepsilon_{\mathrm{kl}}$ and $\bar{\varepsilon}_{\mathrm{pm}}$ represent strain and average strain tensors in V_{RVE_k}. Equation 1c can be used to determine these two strains.

Equation 1a describes the way to compute the microscopic stiffness tensor in an RVE based on the equilibrium at local microscale Eq 1b. After the microscale finite element analyses are completed within the material domain among all the RVEs, the computing results are passed to macroscale:

$$C^{\mathrm{macro}}_{\mathrm{ijpm}} = C^{\Omega}_{\mathrm{ijpm}} = \frac{1}{|V_{\mathrm{macro}}|}\int_{V_{\mathrm{macro}}} C^{\mathrm{micro}}_{\mathrm{ijkl}} L^{\mathrm{macro}}_{\mathrm{klpm}}\mathrm{d}V_{\mathrm{macro}} = \frac{1}{|\Omega|}\int_{\Omega} C^{\mathrm{RVE}}_{\mathrm{ijkl}} L^{\Omega}_{\mathrm{klpm}}\mathrm{d}\Omega, \tag{Eq 2a}$$

$$\begin{aligned}\int_{V_{\mathrm{macro}}} C^{\mathrm{micro}}_{\mathrm{ijpm}}\varepsilon_{\mathrm{ij}}(v^{\mathrm{macro}})\varepsilon^{\mathrm{qs}}_{\mathrm{pm}}(u^{\mathrm{macro}})\mathrm{d}V_{\mathrm{macro}} &= \int_{\Omega} C^{\mathrm{RVE}}_{\mathrm{ijpm}}\varepsilon_{\mathrm{ij}}(v^{\Omega})\varepsilon^{\mathrm{qs}}_{\mathrm{pm}}(u^{\Omega})\mathrm{d}\Omega \\ &= \int_{\partial V_{\mathrm{macro}}} \lambda v_i^{\mathrm{macro}}((u_i^{\mathrm{macro}})^{\mathrm{qs}} - (d_i^{\mathrm{macro}})^{\mathrm{qs}})\mathrm{d}\partial V_{\mathrm{macro}} \\ &\int_{\partial\Omega} \lambda v_i^{\Omega}((u_i^{\Omega})^{qs} - (d_i^{\Omega})^{qs})\mathrm{d}\partial\Omega,\end{aligned} \tag{Eq 2b}$$

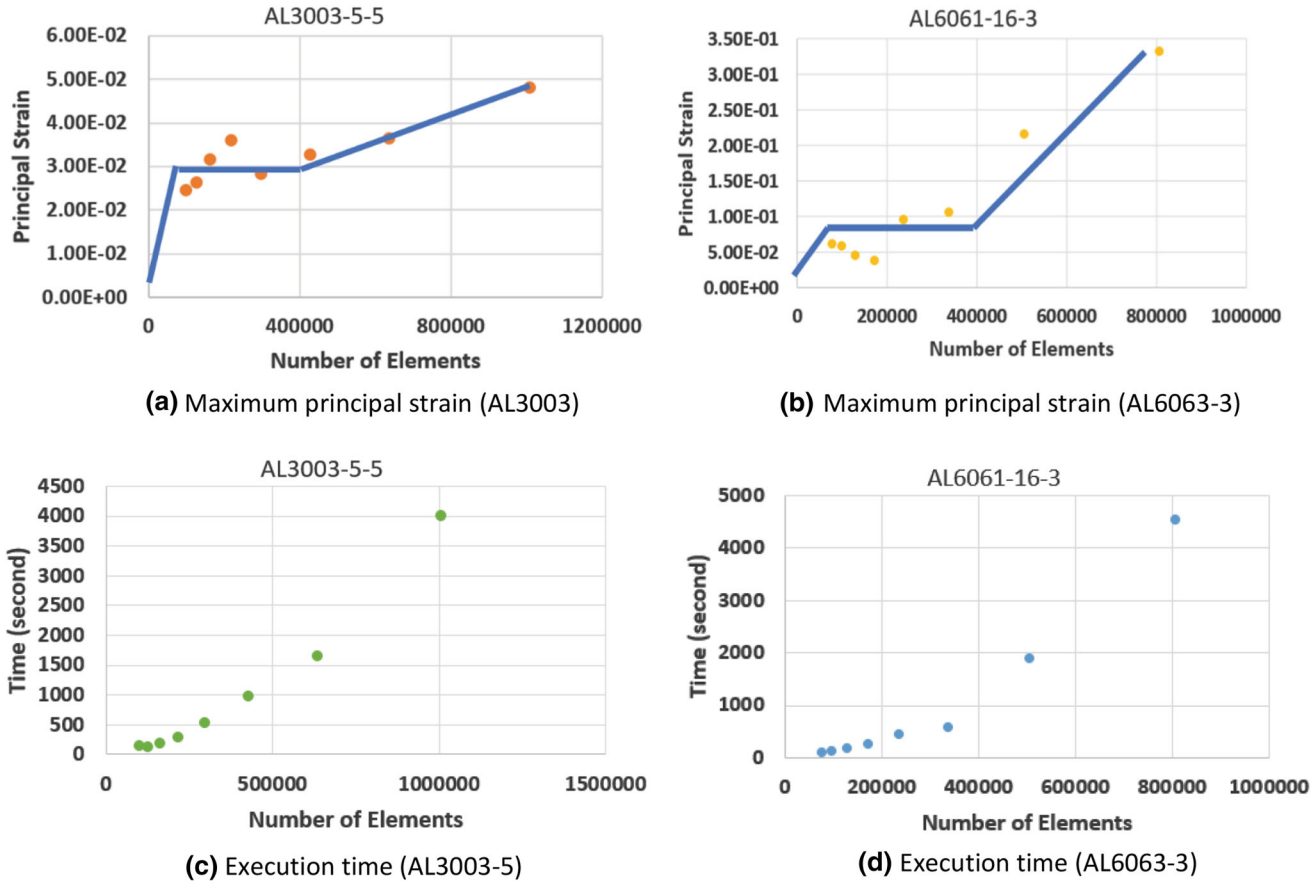

Fig. 3 The relationship between the maximum principal strain and mesh density in the context of reconstructed meshes with various material defects. (Computation was conducted on an ASUS G752VT computer with 32GB RAM, 8 processors, and an NVIDIA Geforce GTX.)

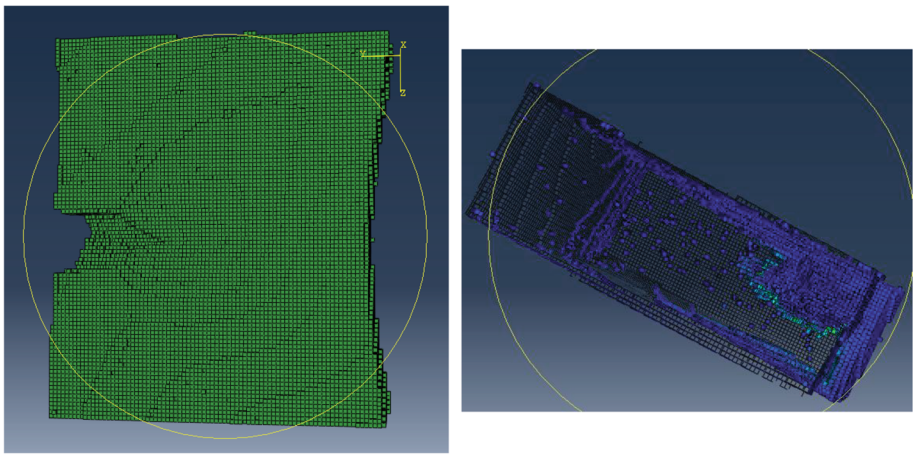

Fig. 4 Adaptive volume meshing of a material domain (216,353 elements)

where $\varepsilon_{kl}^{macro} = L_{klpm}^{macro}\bar{\varepsilon}_{pm}^{macro}$. Superscript and subscript "macro" represent quantities at the macroscale. Ω is the domain of material specimens at the macroscopic scale.

Chow and Lu (Ref 59) proposed an elastic energy equivalence hypothesis: A damaged volume of material under the applied stress has the same elastic energy as the undamaged one submitted to the effective stress, $\tilde{\sigma}$. After the effective Young's modulus of the specimens is computed at the macroscopic scale, our multiscale fatigue damage index based on this hypothesis is defined as

$$\mathrm{MFDI} = 1 - \sqrt{\frac{\overline{E}_{\mathrm{macro}}}{E_0}} \qquad \text{(Eq 3)}$$

where MFDI is our fatigue damage index for quantifying the damage degree of materials due to fatigue. E_0 stands for the

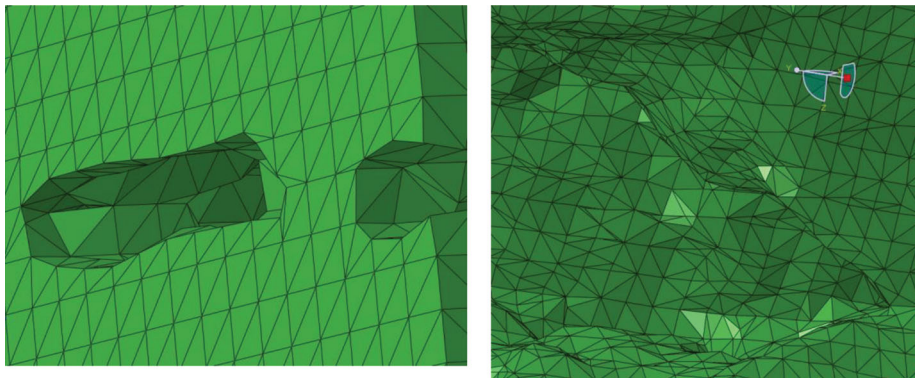

Fig. 5 Results of meshing small defects

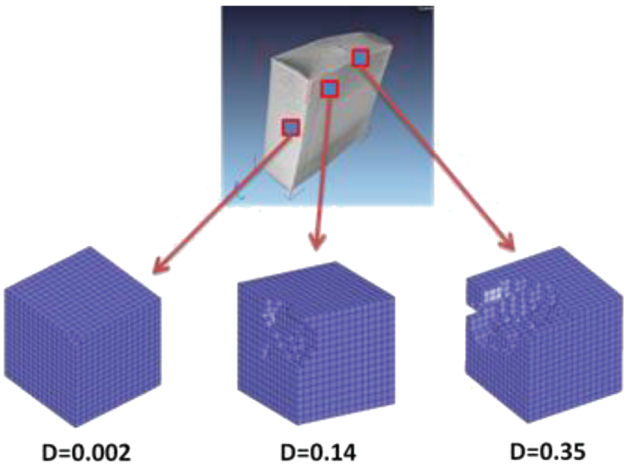

Fig. 6 Local volume models of three RVEs with different degrees of material damage. (D is defined as 1.0-effective area/total area.)

Young's modulus in the undamaged state, and $\overline{E}_{\text{macro}}$ refers to the effective elastic modulus computed from the aforementioned multiscale finite element analysis through $C^{\text{macro}}_{\text{ijpm}}$ in Eq. (2a). Equation (3) is for single axial cases. In multiaxial cases, multiple MFDI_i (i=1,2,3) can be obtained with different loading conditions.

One way to represent fatigue material damage is the use of a 3 x 3 matrix, **[MFDI],** which is similar to a 3 x 3 damage matrix **[D]** in Ref 60, 61. The eigen-values of **[MFDI]** are written as MFDI_k (k=1,2,3), which denotes the fatigue damage values in three orthogonal principal directions of **[MFDI]**. The damage effect matrix, **[M]**, is a 6 x 6 matrix representation for effective stress equation:

$$\{\tilde{\sigma}\} = [\mathbf{M}(\mathbf{MFDI})]\{\boldsymbol{\sigma}\}, \qquad \text{(Eq 4a)}$$

where $\{\tilde{\boldsymbol{\sigma}}\}$ and $\{\boldsymbol{\sigma}\}$ are two 6 x 1 vectors for effective stress and conventional stress, respectively. These two vectors take the following forms:

$$\{\tilde{\sigma}\} = [\,\tilde{\sigma}_{11} \quad \tilde{\sigma}_{22} \quad \tilde{\sigma}_{33} \quad \tilde{\sigma}_{23} \quad \tilde{\sigma}_{13} \quad \tilde{\sigma}_{12}\,]^T,$$

$$\{\boldsymbol{\sigma}\} = [\,\sigma_{11} \quad \sigma_{22} \quad \sigma_{33} \quad \sigma_{23} \quad \sigma_{13} \quad \sigma_{12}\,]^T.$$

$[\mathbf{M}(\mathbf{MFDI})]$ means that **[M]** is dependent upon **MFDI** and could at most have 21 independent components if symmetry of **[M]** is taken into account. To another extreme it may depend upon only one scalar value ($\text{MFDI} = \text{MFDI}_k, \quad k = 1, 3$) in isotropic cases. In anisotropic damage, **[M(MFDI)]** in its principal directions could be simplified into the form below by following the spirit in Ref 62:

$$[\text{M(MFDI)}] = \begin{bmatrix} \frac{1}{1-\text{MFDI}_1} & 0 & 0 & 0 & 0 & 0 \\ 0 & \frac{1}{1-\text{MFDI}_2} & 0 & 0 & 0 & 0 \\ 0 & 0 & \frac{1}{1-\text{MFDI}_3} & 0 & 0 & 0 \\ 0 & 0 & 0 & \frac{1}{\sqrt{(1-\text{MFDI}_2)(1-\text{MFDI}_3)}} & 0 & 0 \\ 0 & 0 & 0 & 0 & \frac{1}{\sqrt{(1-\text{MFDI}_3)(1-\text{MFDI}_1)}} & 0 \\ 0 & 0 & 0 & 0 & 0 & \frac{1}{\sqrt{(1-\text{MFDI}_1)(1-\text{MFDI}_2)}} \end{bmatrix}, \qquad \text{(Eq 4b)}$$

where MFDI_i (i=1,2,3) refer to the fatigue damage indices in three principal directions.

3.5 A New Prognosis Method for Fatigue Residual Life

Let N_r be the fatigue residual life at a particular damage state after a part or structure undergoes a certain number of loading cycles. Here, the fatigue residual life denotes the

remaining number of cycles before the final rupture of the part or structure. Let N_f be the fatigue life of a part or structure under a certain load condition. Then, we propose the following formula to predict N_r under the same load condition:

$$N_r = N_f \cdot (1 - \mathrm{MFDI}), \quad \text{(Eq 5)}$$

where MFDI is our multiscale fatigue damage index determined by Eq. 3. This equation facilitates us to perform the digital diagnosis of fatigue residual life based on x-ray CT data. It has also a potential to be applied in other nondestructive inspection methods.

3.6 Existing Models for Fatigue Life

The Brown-Miller model is a reputed method for predicting fatigue life. The key idea of this approach is that the maximum fatigue damage occurs on a critical plane on which the maximum shear stress or strain is located, and the material damage is contributed by both shear strain and normal strain on this plane. One version of the Brown-Miller model (Ref 63) is expressed by

$$\frac{\Delta\gamma_{\max}}{2} + \frac{\Delta\varepsilon_n}{2} = 1.65\frac{\sigma_f'}{E}(2N_f)^b + 1.75\varepsilon_f'(2N_f)^c, \quad \text{(Eq 6)}$$

where $\Delta\gamma_{\max}$ and $\Delta\varepsilon_n$ are the increments of shear and tensile strains with respect to the critical plane. E is Young's modulus, and $2N_f$ is the endurance in reversals. σ_f' and ε_f' are the fatigue strength and ductility coefficients, respectively. b and c are, respectively, the fatigue strength and ductility exponents.

The principal strain model is another typical criterion, which assumes that fatigue cracks initiate from the plane where the largest principal strain is located. It can be expressed as

$$\frac{\Delta\varepsilon_1}{2} = \frac{\sigma_f'}{E}(2N_f)^b + \varepsilon_f'(2N_f)^c, \quad \text{(Eq 7a)}$$

where $\Delta\varepsilon_1$ is the increment of the largest one among three principal strains. Morrow (Ref 9) proposed a mean stress correction based on an observation that the mean stress effect is more predominant in high cycles, i.e., in elasticity. Equation (2a) is then modified into

$$\frac{\Delta\varepsilon_1}{2} = \frac{(\sigma_f' - \sigma_m)}{E}(2N_f)^b + \varepsilon_f'(2N_f)^c, \quad \text{(Eq 7b)}$$

where σ_m denotes the mean stress. A similar correction can be applied to Eq. (6).

In this paper, for the first time, we utilize our new virtual-physical system (Sect. 3.1) to provide a coordinated comparison between these two models and our new multiscale fatigue damage index.

4. Experiment

4.1 Test Setting

A GE Nanotom x-ray CT system was used for acquiring the defects and damage distribution within each material test specimen. It is a sub-micro computed tomography system with a 2300-by-2300 pixel flat panel detector and a 180 kV x-ray source. With the size of samples in Fig. 7, the scanning resolution is about 2.5 μm per pixel. Two types of aluminum alloys (AL 3003 and 6061) were tested on an MTS machine.

The overall coordinated testing procedures in this study are given below:

(1) For each type of aluminum alloy, several material specimens were tried to determine the fatigue failure cycles at different loading conditions (load-controlled). Based on the test results, a loading condition is selected to target the fatigue failure cycles beyond 50,000 cycles for AL 3003 and 100,000 cycles or 160,000 cycles for AL 6061.
(2) Thirteen materials specimens were tested with the detailed settings shown in Table 4. Each material specimen underwent 4 or 5 different fatigue loading stages, which correspond to x-ray CT inspection points.
(3) In the first group of AL 3003 specimens, 10,000, 20,000, 30,000, 40,000, and 50,000 cycles were used as designated loading stages where the specimens were unloaded from the MTS machine for x-ray CT scanning and then reloaded to the MTS machine for continuing the fatigue test till the next inspection point.
(4) For the second group of AL 6061 specimens, two different fatigue loadings were used. With loading 1, 20,000, 40,000, 60,000, 80,000, and 100,000 cycles were used; under loading 2, 40,000, 80,000, 120,000, and 160,000 cycles were chosen. These cycles corresponded to XCT inspection points.

Figure 7 shows a set of test specimens and the geometric specification of test specimens. Since it is quite time consuming and costly with the XCT scanning, we conducted coordinated tests on only 13 specimens (listed in Table 4) from a batch of 55 specimens (shown in Fig. 7). The design of the materials test specimens was carried out according to Section 03—Metals Test Methods and Analytical Procedures, ASTM standards, with the actual size of specimens being scaled down slightly. Table 5 gives some parameters of these two materials.

4.2 A New Incremental Evaluation Method for Different Methods of Fatigue Life

In detail, the material domains of each test specimen at different loading stages are explicitly described in terms of material defects (voids and cracks). Then, different fatigue life models are incrementally applied to evaluate the accuracy of predicting the fatigue life.

In terms of fatigue damage evaluation, it is difficult to determine the exact fatigue life of each specimen before real materials testing because of the variation of material properties (fatigue scatters). In this study, we devise an incremental evaluation scheme. The basic idea is that we set the x-ray CT inspection intervals at a certain number of cycles (e.g., 10,000 cycles). If we have an inspection sequence: n_1, n_2, …, n_t, then we can approximately assume the fatigue life for this particular specimen is

$$N_f = n_t + m, \quad \text{(Eq 8)}$$

where m refers to half of the cycles between two consecutive inspection points. Given $N_f = n_t + m$, we are ready to evaluate different prediction methods for fatigue life over the results of real materials tests. For the convenience of correlation study in section 5, we introduce a normalized life, which is defined as

$$\widehat{n_i} = \frac{n_i}{N_f}, i = 1, 2, \ldots, t, \quad \text{(Eq 9)}$$

where t refers to the last inspection point before rupture.

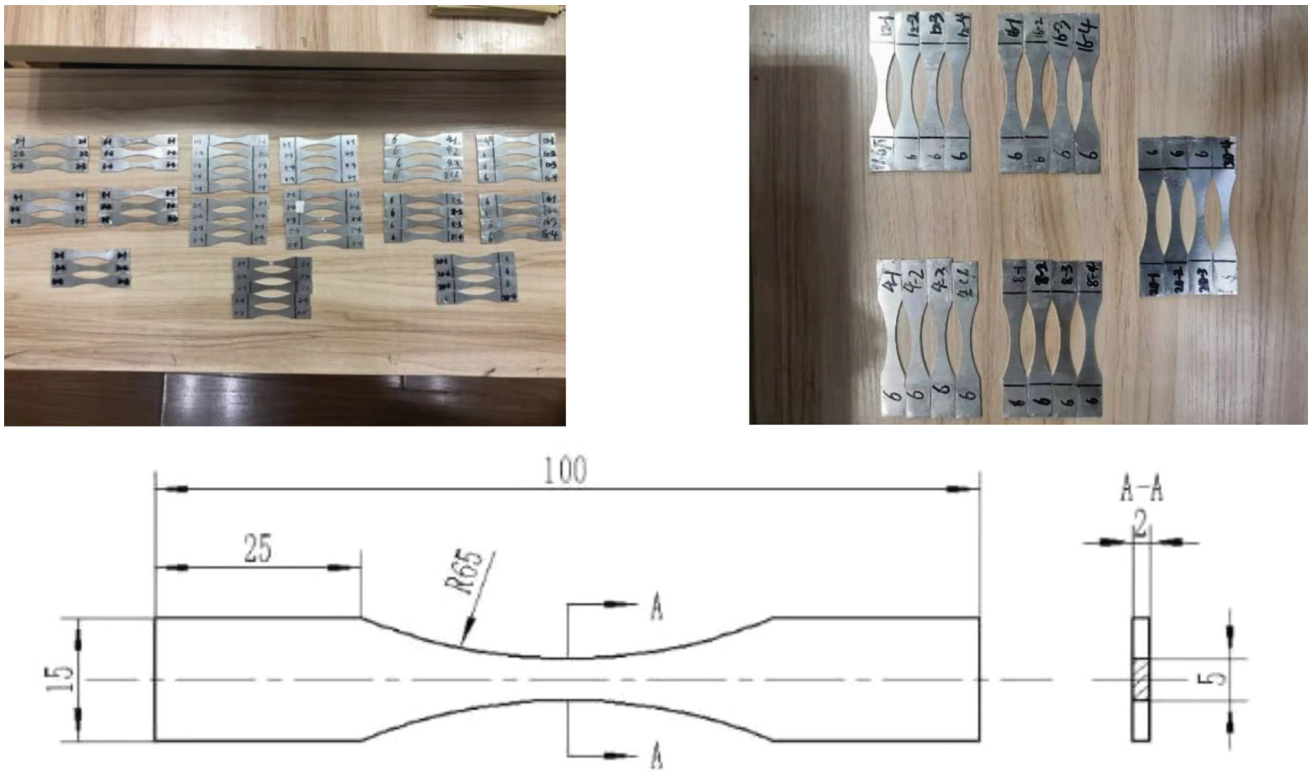

Fig. 7 Materials specimens for the fatigue tests (Dimensions in mm)

Table 4 test setting of AL 3003 and 6061 specimens

material	Load, n	stress ratio, r	load frequency, hz	# of specimens	loading stages (1000 cycles)
AL 3003	1500	0.1	55	5	10, 20, 30, 40, 50
AL 6061	3600	0.1	55	4	20, 40, 60, 80, 100
AL 6061	3300	0.1	55	4	40, 80, 120, 160

Table 5 material parameters of AL 3003 and 6061

material	Young's Modulus, GPa	Poisson's ratio	yield strength, MPa	Ultimate strength, MPa	Density, g/cm3	fatigue strength, MPa	Elongation, %	fracture toughness, MPa $M^{1/2}$
AL 3003	70	0.33	186	200	2.8	55	10	62
AL 6061-T6	68.9	0.33	241	290	2.7	96.5	12-17	29

5. Simulation and Discussion

All the computation in this paper was conducted on an ASUS G752VT computer with Intel i7-6700HQ CPU (4 cores and 8 logical processors) and 32 GB RAM. VG Studio 3.3 was used to visualize x-ray CT data. An in-house C++ code was developed to compute our new multiscale fatigue damage index and predict the fatigue life of the specimens. We weighed the high computational efficiency of C++ language over other programming languages such as Python and Java. Our program contains several modules: a) file I/O of XCT scanning images, b) noise filtering, c) defect detection, d) finite element meshing, and e) digital prognosis. In addition, Abaqus software was also used for finite element analyses.

Figure 8 illustrates x-ray CT models and reconstructed finite element models of two specimens at their final inspection points, which are close to rupture during the high-cycle fatigue tests. The load and boundary conditions as well as von Mises stress distribution are given in Fig. 9. Note that the stress levels in this figure are directly dependent upon the magnitude of the

pseudoloads applied at the far end of the material domain and the fictitious loads in the analysis are used only for the sake of digital prognosis.

From Fig. 10, through 12, we can make the following comments:

Comment 1 The study in this paper represents one of the first attempts to utilize the methodology in Table 1 for a precise investigation on the correlation between fatigue residual life and measured micro- and meso-scale voids and cracks.

Comment 2 Our multiscale fatigue damage index (MFDI) is very strongly correlated with the fatigue life at a confidence level $p = 0.01$ (2-tailed). MFDI is determined by Eq. (3) and related multiscale analyses.

Comment 3 The Brown-Miller model with Morrow's mean stress correction is fairly related to the fatigue life with AL 3003 but not AL 6061. Overall, the Brown-Miller model is one of the best existing models and can produce some reasonable prediction of fatigue life of AL 3003 without any normalization. On the contrary, the principal strain criterion with Morrow's mean stress correction performs poorly even with a normalization (Fig. 11a). In that case, the principal strain criterion tends to have an unclear pattern with the normalized cycles. Both the Brown-Miller model and the principal strain criterion perform poorly with AL 6061, no matter in the format of log life or just estimated life, as shown in Fig. 12.

Comment 4 For the conventional damage mechanics (Ref 30, 64), we use the following formula to calculate the damage variable:

$$d_c = \frac{A - \overline{A}}{A}, \qquad \text{(Eq 10)}$$

where d_c is a damage variable, A is the initial cross section of a part, and $\overline{A}$ represents an effective cross section area after deducting the damaged regions. In this paper, we search a plane where d_c becomes the maximum. d_c ranges between 0.0 and 1.0, corresponding to no damage and full damage, respectively. In terms of correlation with the fatigue damage, the conventional damage mechanics, d_c, performs reasonably well. But, the value of the damage variable is just 0.34 for only 9% of fatigue life to be remained, as illustrated in Fig. 11(b).

Comment 5 By considering not only the correlation but also the value range of each fatigue damage predictor, our ranking on the sequence of excellence from the best to the worst is our multiscale prognosis method, the Brown-Miller model with Morrow's correction, conventional damage mechanics, and principal strain model with Morrow's correction.

Comment 6 It is true that a monotonic pattern should be there if a pure theoretical model is used because fatigue damage is monotonically increasing. This paper focuses on the cases where the prior knowledge of past loading or displacement history is not available. We rely upon a nondestructive measurement to estimate the current state of material fatigue damage. Different models would cause a zigzag pattern to a certain degree. It is our effort to design one method that causes the smallest magnitude of zigzags in the context of predicting residual life.

Comment 7 For AL 3003, Fig. 11(a) shows almost no correlation between principal strain method with Morrow's mean stress correction and the normalized life cycles, while Fig. 11(b) indicates that conventional damage mechanics is insensitive to the normalized cycles during its first half range [0.0, 0.5]. As to AL 6061, our multiscale fatigue damage index has a clearly linear relation with the normalized cycles (Fig. 12a), compared to the poor correlation between the Brown-Miller method (Fig. 12b)/principal strain (Fig. 12c) and the normalized cycles.

Comment 8 Fatigue damage at each XCT inspection point (such as 200,000 cycles in Fig. 13) is estimated by the numerical result of our digital prognosis method based on a material domain model with internal damage information that is determined from XCT scanning results. Our XCT-predicted fatigue damage was compared to the real fatigue damage obtained from MTS testing of the specimens, as shown in Fig. 12(a). In this figure, the horizontal axis refers to the real

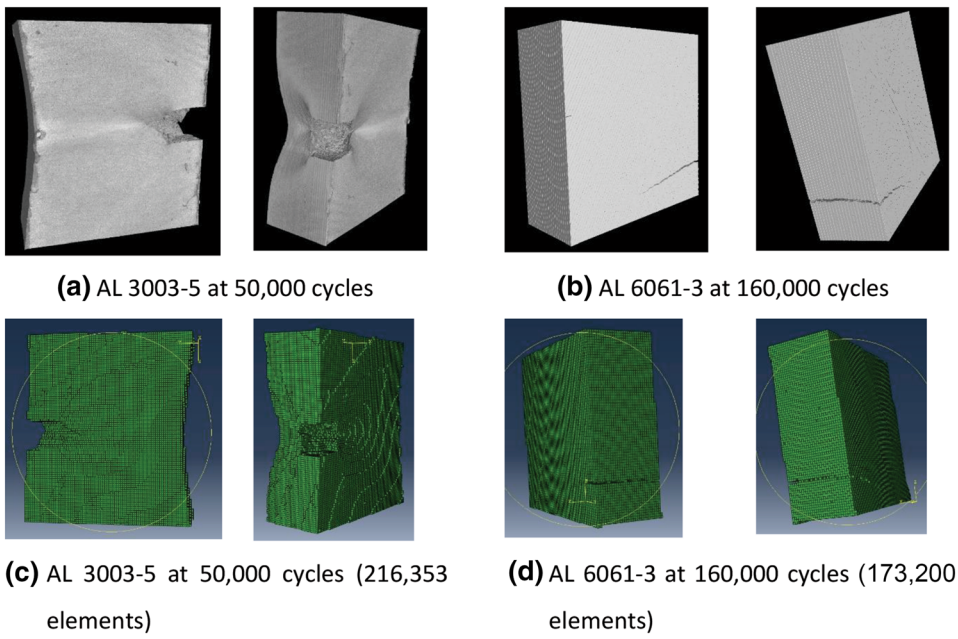

Fig. 8 X-ray CT models and finite element models of two materials test specimens (volume of material domain: 2x5x6.5 mm^3)

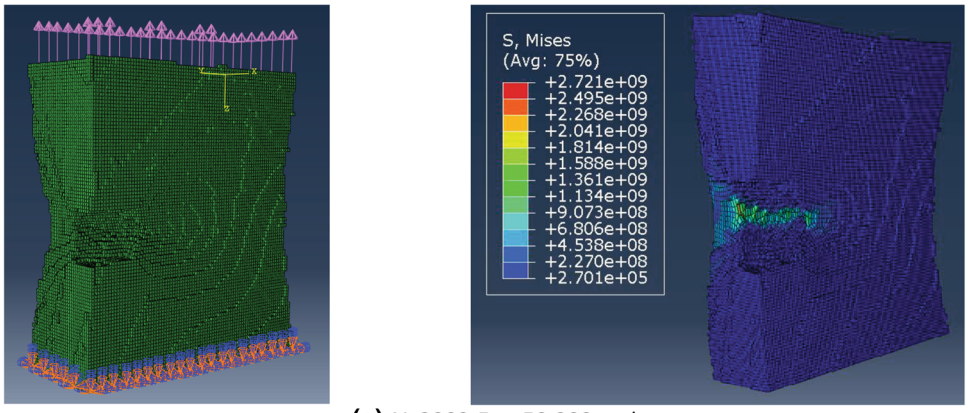

(a) AL 3003-5 at 50,000 cycles

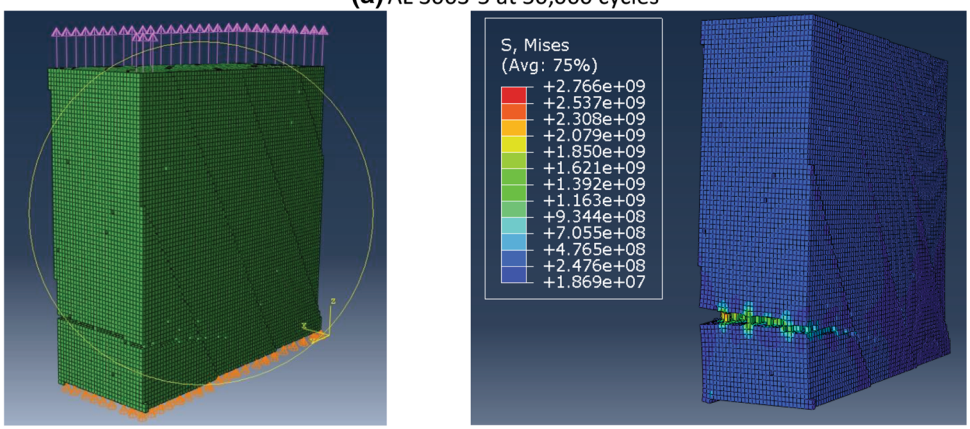

(b) AL 6061-3 at 160,000 cycles

Fig. 9 Load and boundary conditions as well as von Mises stress distribution of two specimens (stress unit: Pascal; a single-step vertical load; volume of material domain: 2x5x6.5 mm^3)

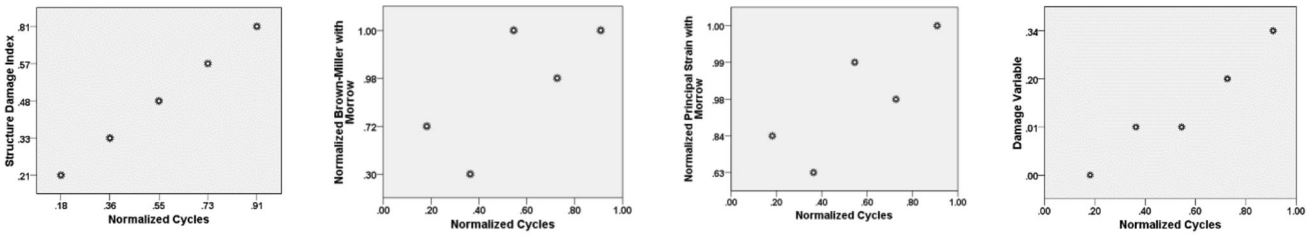

(a) Our fatigue damage index, *MFDI* (r =0.987, p=0.002)

(b) The Brown-Miller model with Morrow's mean stress correction (r=0.651, p= 0.234)

(c) Principal strain with Morrow's mean stress correction (r=0.668, p= 0.217)

(d) Conventional damage variable (r =0.899, p =0.038)

Fig. 10 Bivariate correlation between fatigue life of AL 3003 and different prediction indices. (*r* refers to Pearson correlation, and *p* denotes confidence level.)

MTS fatigue test result, while the vertical axis denotes our XCT-predicted fatigue damage.

Comment 9 Note that the stress distribution in Fig. 9 was the result of a linear elastic analysis that was purely used to estimate the damage state at each XCT inspection point. In other words, we did not use an elasto-plastic analysis to estimate the damage stage or to simulate a damage evolution process (i.e., crack propagation). Therefore, some stress levels in Fig. 9 are greater than the yield stress/ultimate stress of the material because only the Young's modulus is involved in the linear elastic analysis. The reason why we chose the linear elastic analysis is that our index (MFDI) is stress-invariant. In summary, the stress in Fig. 9 does not represent a real stress distribution in an elasto-plastic analysis, and it is just a by-

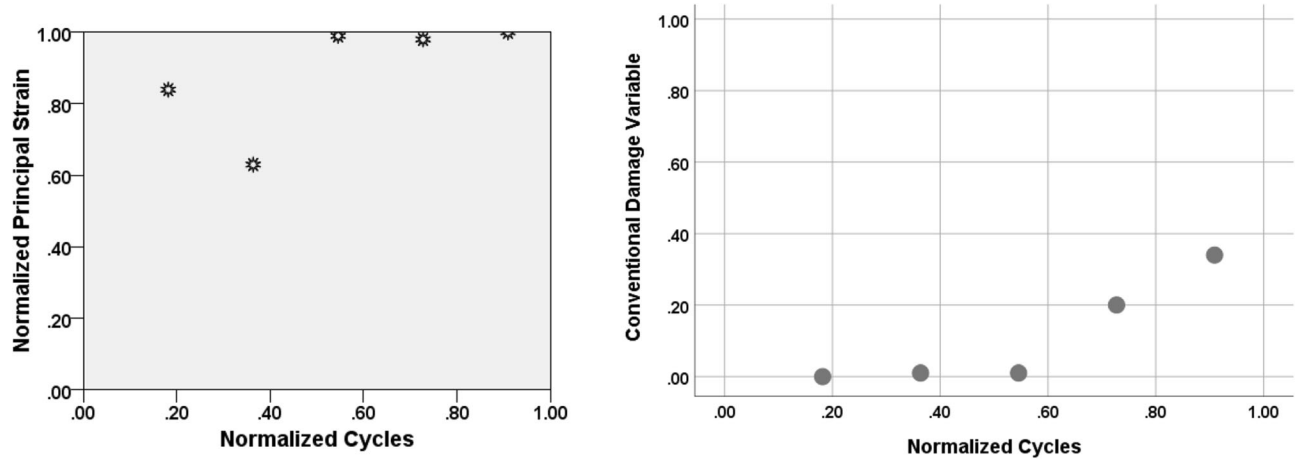

(a) Principal strain with Morrow's mean stress correction

(b) Conventional damage variable

Fig. 11 Bivariate correlation between fatigue life of AL 3003 and different prediction indices (principal strain criterion and conventional damage variable) with the vertical axis rescaled to a range [0.0, 1.0]

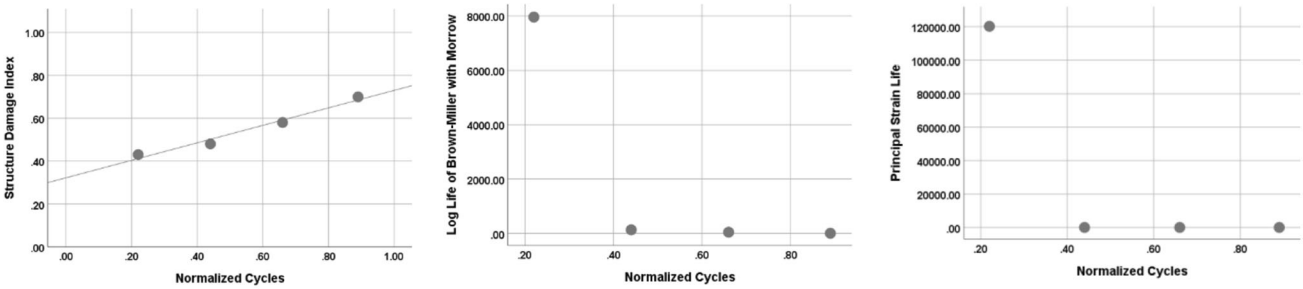

(a) Our multiscale fatigue damage index, *MFDI* (r =0.987, p=0.013)

(b) Log life estimated by the Brown-Miller model with Morrow's mean stress correction (r=-0.778, p= 0.222)

(c) Fatigue life estimated by the principal strain criterion with Morrow's mean stress correction (r=-0.77, p= 0.23)

Fig. 12 Bivariate correlation between fatigue life of AL 6061 and different prediction indices. (*r* refers to Pearson correlation, and *p* denotes confidence level.)

product in our digital prognosis scheme for estimating the current fatigue damage state.

Figure 13 and 14 demonstrates the measured evolution of fatigue damage of AL 3003 in the form of finite element models. The results from AL 6061 are illustrated in Fig. 15 in a format of volume rendering. The visual inspection of Fig. 15 through 15(c) could not provide a difference of the material domain that has underwent 40,000 cycles through 120,000 cycles. During this period, the fatigue damage is microscopic and occurs at the interior of the material domain. It shows the importance of an effective digital diagnosis method for early forecasting of the residual life.

Fatigue damage is a complex process due to various failure patterns (brittle, ductile, rheological, strain-rate-dependent, and temperature-dependent). Furthermore, fatigue life depends upon many factors such as manufacturing defects (fatigue scatters), mean stress level, compressive/tensile stress range, and high-cycle/low-cycle fatigue. Although our method was tested only in a limited scope, the evaluation results are very promising. From Fig. 10 through 12, it can be inferred that our new multiscale fatigue damage index may serve as an ideal fatigue damage signature to predict the fatigue residual life based on Eq 5. According to the best knowledge of the authors in this paper, this is the first successful case in which the authors accurately predicted the fatigue residual life without prior knowledge of load history. This advance may open avenues for precise nondestructive prognosis of fatigue residual life of different materials.

From a scientific point of view, although many experimental standards and data are available in the public domain and very useful in engineering practice, little information is known about the exact void and crack evolution inside a fatigue specimen and how it contributes to the change in its fatigue life in a precise way. The authors hope that our method will serve as a tool to facilitate and promote research activities in such directions.

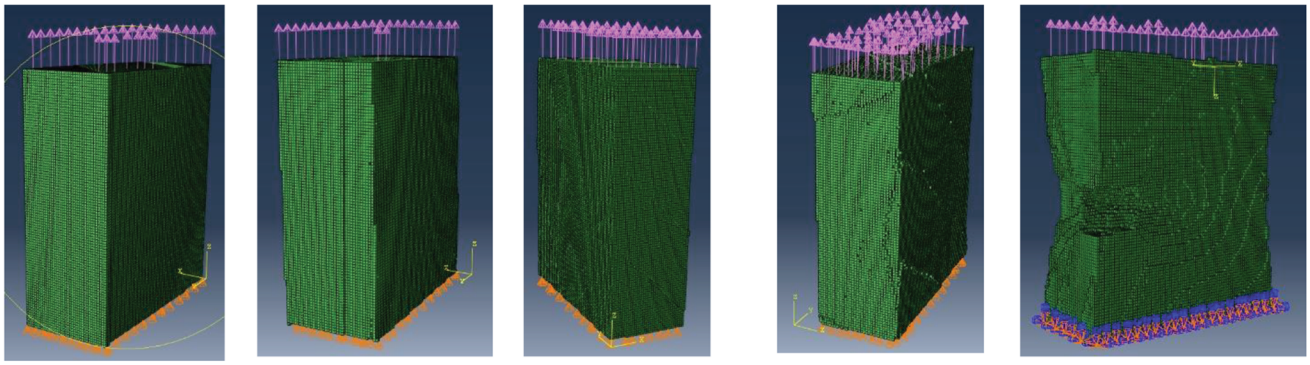

Fig. 13 Fatigue damage evolution of AL 3003 specimen 3 in the format of finite element models with respect to loading and boundary conditions (fatigue load: 1,500 N; fatigue stress ratio: 0.1; fatigue load frequency: 55 Hz; volume of material domain: 2x5x6.5 mm^3)

Our ultimate goal is to develop an onsite nondestructive method to interrogate the current damage state of parts or components in service. Since the lifespan of many parts or components is over 10 years and the past service data may be incomplete or missing, it is crucial to have an onsite measurement method to estimate the current state of these parts or components. In these cases, the exact location at S-N curves is not known because we do not have prior knowledge of past loading or displacement history. How to extend expensive x-ray measurement to inexpensive ultrasonic sensing or other measurement modes will be a study subject in the future. Nevertheless, this study provides the first step toward this direction.

6. Conclusions and Future Research

In this paper, we developed a novel digital prognosis method for predicting the fatigue residual life based on materials defects and damage via a new multiscale fatigue damage index. We also designed an effective way to handle multi-billion-element x-ray CT models and implemented it as an in-house C++ code. A series of coordinated materials fatigue tests and numerical simulations were conducted. The experiment results indicate that our proposed digital prognosis method is significantly better than the state of the art (the Brown-Miller model with Morrow's mean stress correction, principal strain model with Morrow's mean stress correction, and traditional damage mechanics). In a more accurate term, our computational methodology in this paper is the only numerical scheme that has a very strong relationship with the normalized fatigue residual life (|Pearson correlation coefficient| $>$ 0.9). For the first time, the authors numerically and experimentally prove that it is feasible to precisely predict the macroscopic fatigue residual life at any service point of test specimens without relying on the availability of load history. In the evaluation, a new incremental fatigue life evaluation was devised for our coordinated multi-stage testing.

We limit our effort on single-constituent materials, but this method is ready to be applied to evaluate composites as one of our future research activities. Moreover, the evaluation on 3D-printed specimens or samples from any additive manufacturing would be another interesting endeavor to explore. Although we limit ourselves to x-ray CT scanning in this study, the methodology developed here can be equally applied to process a stack of images from SEM or FIB scanning. Due to the restriction of time and funding, this study made only an explorative investigation on the proposed approach. Note that any definitive conclusion should be drawn from a large scale of tests with statistical nature estimated. This will be a topic of future work. Furthermore, it is a well-known fact that considerable changes of residual fatigue lives are observed with random sequence of fatigue loading. Further work is needed to determine how well the proposed MFDI method can be applied to this situation.

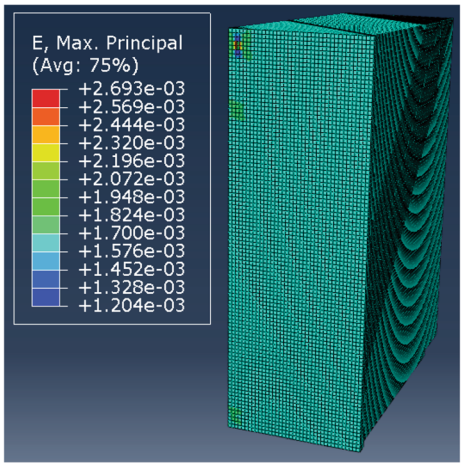

(a) 100,000 cycles (Node: 354,328; Elements:337,630)

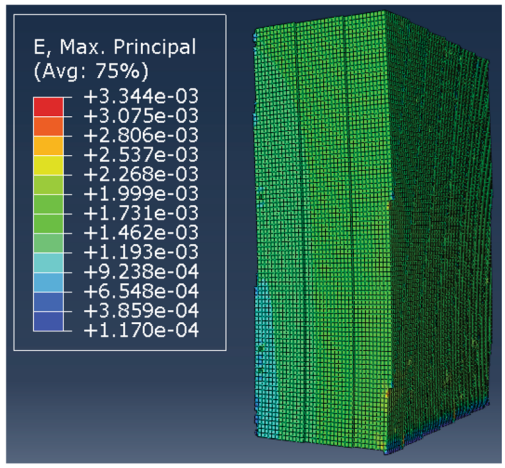

(b) 200,000 cycles (Node: 308,168; Elements: 292,352)

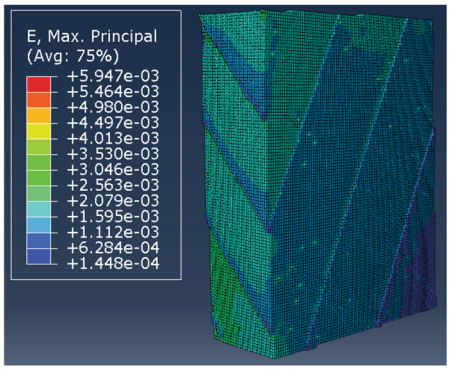

(c) 300,000 cycles

(Node: 372,946; Element: 354,800)

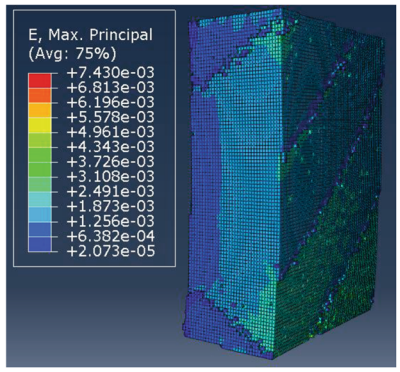

(d) 400,000 cycles (Node: 280,046; Elements: 231,059)

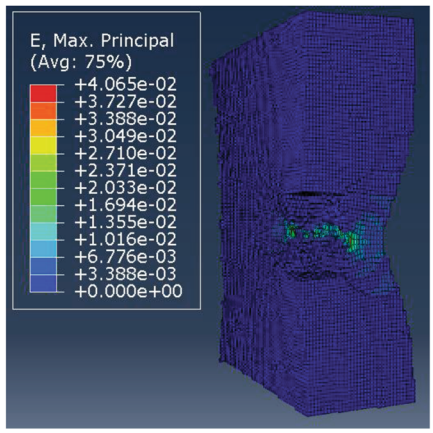

(e) 500,000 cycles

(Node: 237,105; Element: 217,648)

Fig. 14 Fatigue damage evolution of AL 3003 specimen 3 in the format of finite element models with respect to maximum principal strain (fatigue load: 1,500 N; fatigue stress ratio: 0.1; fatigue load frequency: 55 Hz; volume of material domain: 2x5x6.5 mm^3)

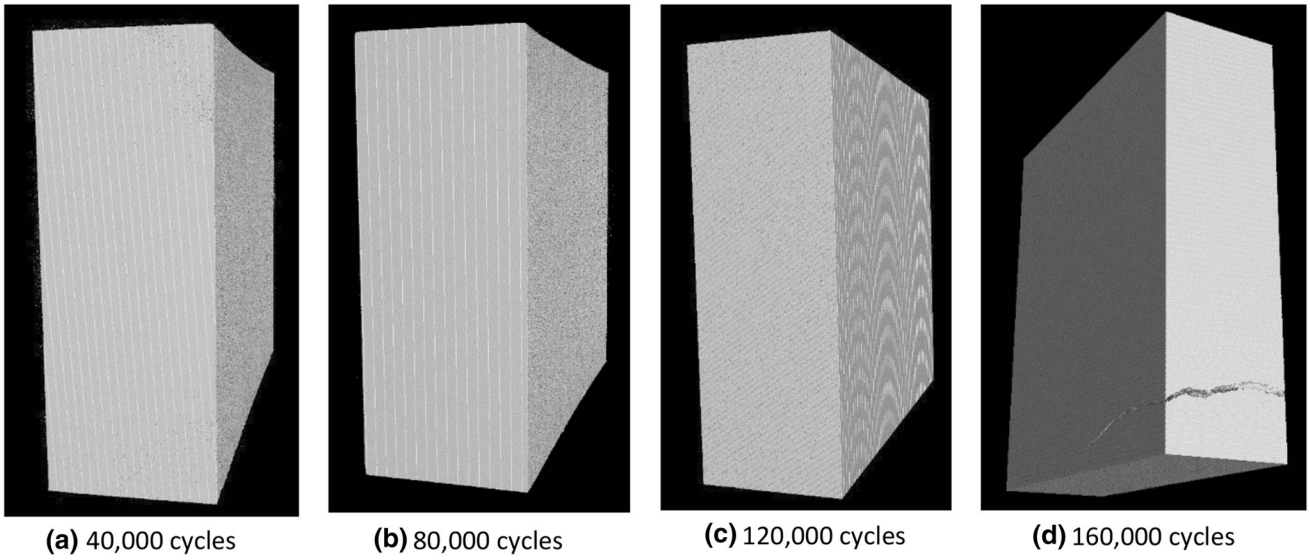

Fig.15 Fatigue damage evolution of AL 6061 specimen 1 in the format of volume rendering (volume of material domain: 2x5x6.5 mm^3)

Acknowledgments

This study was supported in part by U.S. National Science Foundation grants (DMI-0514900, CMMI-0721625, ECCS-1039563, and IIP-1445355). The authors would like to express their sincere gratitude to the three anonymous reviewers for their comments, which significantly improved the quality of this manuscript.

Data Availability

All the finite element models reported in this article are available from the corresponding author of this article upon request and will also be stored at the University of Michigan Deep Blue Repository (https://deepblue.lib.umich.edu).

Conflict of interest

The authors declare no competing financial or non-financial interests.

References

1. D.D. He, Z.X. Li, H.Q. Sheng and C. Chen, Multi-Scale Experimental Study on Fatigue Damage Behaviour and its Effect on Structural Nonlinear Response, *Fatigue Fract. Eng. Mater. Struct.*, 2013, **36**(2), p 102–114.
2. A.A. Shanyavskiy and A.P. Soldatenkov, Evolution From Micro-to Meso-and Macroscale Level in Metal Fatigue, *AIP Conf. Proc.*, 2019, **2167**(1), p 020324.
3. X.S. Tang and T.T. Wei, Microscopic Inhomogeneity Coupled with Macroscopic Homogeneity: A Localized Zone of Energy Density for Fatigue Crack Growth, *Int. J. Fatigue*, 2015, **70**(1), p 270–277.
4. W. Schutz, A History of Fatigue, *Eng. Fract. Mech.*, 1996, **54**(2), p 263–300.
5. O.H. Basquin, The Exponential Law of Endurance Test, *Proc. Am. Soc. Test. Mater.*, 1910, **10**, p 625–630.
6. M. Matsuishi and T. Endo, *Fatigue of metals subjected to varying stress*, Japan Society of Mechanical Engineers, Fukuoka, 1968
7. M.A. Miner, Cumulative Damage in Fatigue, *J. Appl. Mech.*, 1945, **12**(3), p A159–A164.
8. M.W. Brown and K.J. Miller, A Theroy for Fatigue Failure under Multiaxial Stress-Strain Conditions, *Proc. Inst. Mech. Eng.*, 1973, **187**(1), p 745–755.
9. J. Morrow, *Fatigue design handbook*. Advances in engineering, Vol. 4 (Society of Automotive Engineers, Warrendale, PA, 1968), pp. 21–29
10. T. Palin-Luc and S. Laserre, An Energy Based Criterion for High Cycle Multiaxial Fatigue, *Eur. J. Mech.-A/Solids.*, 1998, **17**(2), p 237–251.
11. S. Suresh, *Fatigue of materials*, Cambridge University Press (Cambridge, United Kingdom, 2001)
12. L.F. Coffin, Some Perspectives on Future Directions in Low Cycle Fatigue, *ASTM Spec. Tech. Publ.*, 1988, **942**, p 5–14.
13. S.S. Manson, Future Directions for Low Cycle Fatigue, *ASTM Spec. Tech. Publ.*, 1988, **942**, p 15–39.
14. D. Socie, Multiaxial fatigue damage assessment. In: Rie, KT. (eds) *Low cycle fatigue and elasto-plastic behaviour of materials.* (Springer, Dordrecht, 1987), pp. 465–472. https://doi.org/10.1007/978-94-009-3459-7_72
15. C.L. Chow and Y. Wei, A Damage Mechanics Model Of Fatigue Crack Initiation in Notched Plates, *Int. J. Theor. Appl. Fract. Mech.*, 1991, **16**(2), p 123–134.
16. K. Dang Van, G. Cailetaud, J. F. Flavenot, A. Le Douaron, H. P. Lieurade, Criterion for high-cycle fatigue failure uner mutilaxial loading. In *Proceedings of ICBMFF2.* (2013), pp. 459-478
17. J. Lemaitre and J.L. Chaboche, *Mechanics of solid materials*, Cambridge University Press (Cambridge, United Kingdom, 1990)
18. B. Bhattacharya and B. Ellingwood, Continuum Damage Mechanics Analysis of Fatigue Crack Initiation, *Int. J. Fatigue*, 1998, **20**(9), p 631–639.
19. S. Kwofie and N. Rahbar, A Fatigue Driving Approach to Damage and Life Prediction under Variable Amplitude Loading, *Int. J. Damage Mech.*, 2013, **22**(3), p 393–404.
20. H. Yanase, K. Shojime and C. Ogata, High Cycle Fatigue Threshold Behaviors in Notched Plates, *Int. J. Damage Mech.*, 2013, **22**(7), p 1006–1022.
21. E. Rejovitzky and E. Altus, On Single Damage Variable Models for Fatigue, *Int. J. Damage Mech.*, 2014, **22**(2), p 268–284.
22. Q.H. Vu, D. Halm and Y. Nodot, High Cycle Fatigue of 1045 Steel Under Complex Loading: Mechanisms Map and Damage Modeling, *Int. J. Damage Mech.*, 2014, **23**(3), p 377–410.
23. X. Xue and X. Yang, A Damage Model for Concrete Under Cyclic Actions, *Int. J. Damage Mech.*, 2014, **23**(2), p 155–177.
24. M. Mashayekhi, T. Taghipour, A. Askari and M. Farzin, Continuum Damage Mechanics Application in Low-Cycle Thermal Fatigue, *Int. J. Damage Mech.*, 2013, **22**(2), p 285–300.
25. S. Kenderian, B.B. Djordjevic and R.E. Green, Point and Line Source Laser Generation of Ultrasound for Inspection of Internal and Surface Flaws in Rail and Structural Materials, *Res. Nondestruct. Eval.*, 2001, **13**(4), p 189–200.
26. C. Dang, L.W. Schmerr and A. Sedov, Modeling and Measuring all the Elements of an Ultrasonic Nondestructive Evaluation System I:

Modeling Foundations, *Res. Nondestruct. Eval.*, 2002, **14**(3), p 141–176.
27. S.C. Wooh and J.Y. Wang, Nondestructive Characterization of Planar Defects using Laser-Generated Ultrasonic Shear Waves, *Res. Nondestruct. Eval.*, 2001, **13**(4), p 215–230.
28. B.H. Kim, K. Heedai and P. Taehyo, Nondestructive Damage Evaluation of Plates Using the Multi-Resolution Analysis of Two-Dimensional Haar Wavelet, *J. Sound Vib.*, 2006, **292**(1–2), p 82–104.
29. I. Iturrioz, G. Lacidogna and A. Carpinteri, Acoustic Emission Detection in Concrete Specimens: Experimental Analysis and Lattice Model Simulations, *Int. J. Damage Mech.*, 2014, **23**(3), p 327–358.
30. J. Lemaitre, *A course on damage mechanics*, Springer, Berlin/Heidelberg, Germany, 1996
31. B. Burks and M. Kumosa, A Modal Acoustic Emission Signal Classification Scheme Derived from Finite Element Simulation, *Int. J. Damage Mech.*, 2014, **23**(1), p 43–62.
32. A.M. Gokhale and S. Yang, Application of Image Processing for Simulation of Mechanical Response of Multi-Length Scale Microstructures of Engineering Alloys, *Metall. Mater. Trans. A.*, 1999, **30**(9), p 2369–2381.
33. S.A. Langer, E.R. Fuller and W.C. Carter, OOF: An Image-Based Finite-Element Analysis of Material Microstructures, *Comput. Sci. Eng.*, 2001, **3**(3), p 15–23.
34. Z. Shan and A.M. Gokhale, Digital image Analysis and Microstructure Modeling Tools for Microstructure Sensitive Design of Materials, *Int. J. Plast.*, 2004, **20**(7), p 1347–1370.
35. A.C. Lewis and A.B. Geltmacher, Image-Based Modeling of the Response of Experimental 3D Microstructures to Mechanical Loading, *Scr. Mater.*, 2006, **55**(1), p 81–85.
36. M.V. Kral and G. Spanos, Three-Dimensional Analysis of Proeutectoid Cementite Precipitates, *Acta Mater.*, 1999, **47**(2), p 711–724.
37. P. Dawson, M. Miller, T. Han and J. Bernier, An Accelerated Methodology for the Evaluation of Critical Properties in Polyphase Alloys, *Metall. Mater. Trans. A.*, 2005, **36**(7), p 1627–1641.
38. A.J. Kubis, G.J. Shiflet, D.N. Dunn and R. Hull, Focused Ion-Beam Tomography, *Metall. Mater. Trans. A.*, 2004, **35**(7), p 1935–1943.
39. J.M. de Oliveira, F.Z.C. de Lima, J.A. de Milito and A.C.G. Martins, Development and Applications of Three-Dimensional Gamma ray Tomography System Using ray Casting Volume Rendering, *Braz. J. Phys.*, 2005, **35**(3B), p 789–792.
40. F. Beckmann, Neutron and synchrotron-radiation-based imaging for applications in material science, *Neutrons and synchrotron radiation in engineering materials science*. W. Reimers, A.R. Pyzalla, A. Schreyer, H. Clemens Ed., Wiley-Vch, Weinheim, Germany, 2008, p 287–307
41. D. Bernard, D. Gendron, J. Heintz, S. Bordere and J. Etourneau, First Direct 3D Visualization of Microstructural Evolutions During Sintering Through X-ray Computed Microtomography, *Acta Mater.*, 2005, **53**(1), p 121–128.
42. K.M. Dobrich, C. Rau and C.E. Krill, Quantitative Characterization of the Three-Dimensional Microstructure of Polycrystalline Al-Sn Using X-ray Microtomography, *Metall. Mater. Trans. A.*, 2004, **35**(7), p 1953–1961.
43. H. Elaqra, N. Godin, G. Peix, M.R. Mili and G. Fantozzi, Damage Evolution Analysis in Mortar, During Compressive Loading Using Acoustic Emission and X-ray Tomography: Effects of the Sand/Cement Ratio, *Cem. Concr. Res.*, 2007, **37**(5), p 703–713.
44. G. Bonifazi, P. Massacci and S. Serranti, Micro-Tomography Techniques Applied to Particulate Solids Based Products Characterization, *Granul. Matter*, 2008, **10**(4), p 315–321.
45. K. Gopalakrishnan, H. Ceylan and F. Inanc, Using X-ray Computed Tomography to Study Paving Materials, *Proc. Inst. Civil Eng. Const. Mater.*, 2007, **160**(CM1), p 15–23.
46. M. Daigle, D. Fratta, L. B. Wang, Ultrasonic and X-ray tomographic imaging of highly contrasting inclusions in concrete specimens. In: *GeoFrontier 2005 Conference.* January 24-26, (Austin, Texas, United States, 2005)
47. L.B. Wang, J.D. Frost, G.Z. Voyiadjis and T.P. Harman, Quantification of Damage Parameters Using X-ray Tomography Images, *Mech. Mater.*, 2003, **35**(8), p 777–790.
48. L.B. Wang, J.Y. Park and Y. Fu, Representation of real particles for DEM simulation using X-ray tomography, *Constr. Build. Mater.*, 2007, **21**(2), p 338–346.
49. N. Burlion, D. Bernard and D. Chen, X-ray Microtomography: Application to Microstructure Analysis of a Cementitious Material During Leaching Process, *Cem. Concr. Res.*, 2006, **36**(2), p 346–357.
50. S. Siddique, M. Imran, M. Rauer, M. Kaloudis, E. Wycisk, C. Emmelmann and F. Walther, Computed Tomography for Characterization of Fatigue Performance of Selective Laser Melted Parts, *Mater. Des.*, 2015, **83**, p 661–669.
51. Y. Nadot, C. Nadot-Martin, W.H. Kan, S. Boufadene, M. Foley, J. Cairney, G. Proust and L. Ridosz, Predicting the Fatigue Life of an AlSi10Mg Alloy Manufactured via Laser Powder Bed Fusion by Using Data from Computed Tomography, *Addit. Manuf.*, 2020, **32**, p 100899.
52. H. Peng, J. Fan, X. Zhang, J. Chen, Z. Li, D. Jiang and C. Liu, Computed Tomography Analysis on Cyclic Fatigue and Damage Properties Of Rock Salt under Gas Pressure, *Int. J. Fatigue*, 2020, **134**, p 105523.
53. J. Shen, D. Yoon, Y. Song, S. Liu, Repairing polygonal meshes for volume meshing. In *Proceedings of Computer Graphics and Virtual Reality 06.* June 26-29, (Las Vegas, Nevada, USA, 2006), pp. 189-195
54. C.L. Chow, J. Mao and J. Shen, Nonlocal Damage Gradient Model for Fracture Characterization of Aluminum Alloy, *Int. J. Damage Mech.*, 2011, **20**(7), p 1073–1093.
55. W. Lorensen and H. Cline, Marching Cube: A High Resolution 3-D Surface Construction Algorithm, *ACM SIGGRAPH Comput. Graph. Proc.*, 1987, **21**(4), p 163–169.
56. A. Lopes and K. Brodlie, Improving the Robustness and Accuracy of the Marching Cubes Algorithm for Isosurfacing, *IEEE Trans. Vis. Comput. Graph.*, 2003, **9**(1), p 16–29.
57. R. Lohner, Progress in Grid Generation via the Advanced Front Technique, *Eng. Comput.*, 1996, **12**, p 186–210.
58. J. Shen, D. Yoon, S. Wei, J. Boileau, J. Mao, W. Shi, J. M. Wells, G. Reyes, C. L. Chow, Material damage estimated via linking micro/-macroscale defects to macroscopic mechanical properties. Int. J. Damage Mech. vol. 23(4) (Thousand Oaks, CA, 2014), pp. 537–566
59. C.L. Chow and T.L. Lu, On Evolution Laws of Anisotropic Damage, *Eng. Fract. Mech.*, 1989, **34**(3), p 679–701.
60. C.L. Chow, M. Jie and X. Wu, A Damage-Coupled Criterion of Localized Necking Based on Acoustic Tensor, *Int. J. Damage Mech.*, 2007, **16**(3), p 265–282.
61. G.Z. Voyiadjis and P.I. Kattan, A Comparative Study of Damage Variable in Continuum Damage Mechanics, *Int. J. Damage Mech.*, 2009, **18**(4), p 315–340.
62. C.L. Chow and M. Jie, Anisotropic Damage Coupled Sheet Metal Forming Limit Analysis, *Int. J. Damage Mech.*, 2009, **18**(4), p 371–292.
63. F.A. Kandil, M.W. Brown and K.J. Miller, *Biaxial low-cycle fatigue of 316 stainless steel at elevated temperatures*, Metals Society, United Kingdom, 1982
64. J. Lemaitre and R. Desmorat, *Engineering damage mechanics*. (Springer, Berlin/Heidelberg, Germany, 2005)